AUTO TEMPLATE ASSEMBLY OF $CACO_3$-CHITOSAN HYBRID NANOBOXES AND NANOFRAMES IN IONIC LIQUID MEDIUM

A Thesis

by

HSINGMING ANNA CHEN

Submitted to the Office of Graduate Studies of
Texas A&M University
in partial fulfillment of the requirements for the degree of

MASTER OF SCIENCE

May 2011

Major Subject: Chemical Engineering

Auto Template Assembly of $CaCO_3$-Chitosan Hybrid Nanoboxes and Nanoframes in Ionic Liquid Medium

AUTO TEMPLATE ASSEMBLY OF $CACO_3$-CHITOSAN HYBRID NANOBOXES AND NANOFRAMES IN IONIC LIQUID MEDIUM

A Thesis

by

HSINGMING ANNA CHEN

Submitted to the Office of Graduate Studies of
Texas A&M University
in partial fulfillment of the requirements for the degree of

MASTER OF SCIENCE

Approved by:

Chair of Committee,	Mustafa Akbulut
Committee Members,	Hae-Kwon Jeong
	Melissa Grunlan
Head of Department,	Michael Pishko

May 2011

Major Subject: Chemical Engineering

ABSTRACT

Auto Template Assembly of $CaCO_3$-Chitosan Hybrid Nanoboxes and Nanoframes in Ionic Liquid Medium. (May 2011)

Hsingming Anna Chen, B.S., The University of Texas

Chair of Advisory Committee: Dr. Mustafa Akbulut

Recently, there has been increased effort in researching methods for producing hollow nanostructures because of their potential impact in the fields of catalysis, separation processes, drug delivery, and energy storage and conversion devices. The purpose of this thesis is to describe a method for forming hollow inorganic-organic hybrid nanoboxes and nanoframes. This approach relies upon ionic liquid (1-butyl-3-methyl-imidazolium chloride) mediated auto-templating assembly of $CaCO_3$ and chitosan to form nanoframes (two open faces) and nanoboxes (one open face).

The average dimension of the nanostructures formed was 339 ± 95 x 299 ± 89 nm. Detailed structure of nanoboxes and nanoframes were obtained by 3-D electron tomography and X-ray diffraction. Chemical bonding was determined by Fourier transform infrared (FTIR) spectroscopy, and the ratio of organics to inorganics in the nanostructures was determined by thermal gravimetric analysis. The chitosan to $CaCO_3$ weigh ratio, mixing strength, temperature, and dialysis time were varied to further elucidate the method of formation. It was found that increasing the mixing power caused

the equilibrium nanostructure dimension to decrease. On the other hand, varying the experimental temperature in the range of 80 to 160˚C did not affect the nanostructure dimension. The dialysis study showed that during dialysis the nanostructure core was increasingly removed. Nanoframes were observed after 72 hours of dialysis. With further dialysis, there was continued erosion of nanoframes. Results indicate that the concentration gradient and the solubility difference between the mixture components were responsible for this transformation.

DEDICATION

For my parents

ACKNOWLEDGEMENTS

I would like to thank my advisor, Dr. Mustafa Akbulut, for all his research guidance; for his confidence in my ability; and for his financial support. Without his support, I would never have been exposed to the field of scientific research. I would like to thank Dr. Luo Zhiping in the Microscopy Center who trained me to use the transmission electron microscope and contributed to my first paper. Moreover, I would like to thank Dr. Yordanos Bisrat, Dr. Amanda Young, and Dr. Zhen Li in the Materials Characterization Facility who trained me to use the various instruments on the third floor, and in several instances advised me on analytical techniques. I would also like to thank Dr. Melissa Grunlan for letting me use the thermal gravimetric analysis (TGA) equipment in her lab, and Dr. Hae-Kwon Jeong for teaching me the theories behind crystallization. Lastly, I would like to thank Dr. Joseph Reibenspies and Dr. Nattamai Bhuvanesh in the chemistry department who helped me analyze the X-ray powder diffraction patterns. I really appreciate all your time spent educating me and sharpening my skills as an engineer and researcher.

TABLE OF CONTENTS

Page

LIST OF FIGURES

1. INTRODUCTION

The purpose of this thesis is to present the results of a yearlong research project on the crystallization of hollow $CaCO_3$-chitosan hybrid nanostructures in an ionic liquid medium. Section one begins with a brief overview of crystal nucleation and growth, a literature review of the current methods of forming hollow nanostructures, and an introduction to the formation of $CaCO_3$-chitosan hybrid nanostructures. Section 2 describes the various material characterization equipment used in this study which include the transmission electron microscopy (3-D electron tomography and single crystal X-ray diffraction), scanning electron microscopy, powder X-ray diffraction, Fourier transform infrared spectroscopy, and thermal gravimetric analysis. This section also gives information on the materials and procedures used in this research project. Section 3 consists of the experimental results and discussion. Lastly, Section 4 concisely summarizes and concludes this thesis.

1.1 Classification of Crystals

Crystals may be categorized into four groups – ionic, molecular, covalent, and metallic. Ionic crystals have ions at the lattice sites which bind to one another by electrostatic forces. The distance between ions is the position of minimal repulsion and maximum attraction. Due to the electrostatic forces, ionic crystals are hard and brittle with high melting points. Molecular crystals have lattice sites that are occupied by atoms or molecules. The smaller the molecules the softer the material and the lower the

---

This thesis follows the style of *Chemical Communications*.

material melting point due to weak intermolecular interactions. Molecular crystals are also bad electrical conductors. Covalent crystals contain atoms at lattice positions held together by covalent bond. They are very hard, poor electrical conductors with high melting points due to the covalent bonding. Some well-known examples of covalent crystals are diamond and quartz. The last category of crystals is metallic crystals that have cations at the lattice positions surrounded by a "sea" of electrons. They are good heat and electric conductors due to the fluid "sea" of electrons.[1]

1.2 Crystallization Methods

Crystallization is the formation of a solid phase with regular repeating atoms, ions, or molecules from a solution, melt, vapor, or from another solid phase.[2] It is an important process in industry for the production of high tech materials such as semiconductors[3] and electrical conductors.[4] In addition, it is used to produce consumer goods on a large scale such as powder food salts[5] and pharmaceutical drugs.[6] Furthermore, it is an indispensible technique used for bulk separation and purification processes.[2]

In the chemical and pharmaceutical industry, batch crystallization is the most commonly used. Batch crystallization is where the addition of pure solute and solvent occurs at the beginning of the process cycle and then product is extracted at the end of the cycle. There are many advantages to using batch crystallization. First of all, the equipment needed is simple and easy to maintain, and batch crystallization may be used to process highly viscous or toxic materials. Moreover, batch crystallizers can produce crystals with smaller size distribution than continuous crystallizers.[7] On the other hand

there are disadvantages to the batch crystallizer which include inconsistency of crystal size, numbers, and purity between batches.[8] There are four types of batch crystallizers – cooling, evaporative, reaction, and salting out. Each method has a different manner of creating solute supersaturation in solution. Cooling crystallization is based on the fact that the solubility of a solute increases with temperature. As the solution is cooled, the solubility will decreases causing a solid phase to form. Evaporative crystallization uses the evaporation of solute at constant temperature to increase the solute concentration above the solubility threshold. Reaction crystallization converts the reactants in solution into a low solubility product. Lastly, salting out crystallization uses the addition of an anti-solvent to decrease the solubility of the solute.[7] Although there are numerous crystallization methods, each involves the steps of nucleation and growth.

1.3 Crystal Nucleation

Nucleation is the first step in forming a crystal. There are two categories of crystal nucleation - homogeneous and heterogeneous nucleation. Homogeneous nucleation is the spontaneous formation of nuclei in a supersaturated solution while heterogeneous nucleation is the formation of nuclei on an existing surface in the supersaturated solution. In both cases the concentration of the solute must be above the equilibrium solubility concentration, in other words the solution must be supersaturated, in order for nucleation to occur. The driving force for both nucleation and growth is the decrease in Gibbs free energy. The change in Gibbs free energy per solid volume formed is expressed as

$$\Delta G_v = -\frac{kT}{\Omega} ln\left(\frac{C}{C_o}\right) = -\frac{kT}{\Omega} ln\, S \quad (1)$$

where c is the solute concentration; c_o is the equilibrium solubility concentration; k is the Boltzmann constant; T is the temperature; Ω is the atomic volume; and S is supersaturation.[9] Nucleation occurs spontaneously when S > 1 and $\Delta G_v < 0$. If one assumes that the nucleus formed has a spherical shape with radius r, the change in Gibbs free energy is

$$\Delta\mu_v = \frac{4}{3}\pi r^3 \Delta G_v. \quad (2)$$

When volume is formed, more surface area is also formed. If γ is the surface energy per surface area, the increase in energy due to the formation of new surface area is given by

$$\Delta\mu_s = 4\pi r^2 \gamma. \quad (3)$$

The summation of equation (2) and (3) gives the total change of chemical potential for homogeneous nucleation, equation (4):

$$\Delta G = \frac{4}{3}\pi r^3 \Delta G_v + 4\pi r^2 \gamma \quad (4)$$

ΔG passes through a maximum (as shown in Fig. 1) at critical energy (ΔG^*) and critical size (r^*). The critical energy and cluster size are given by equations (5) and (6), respectively. ΔG^* is the energy barrier that must be overcome for nucleation to occur, and the critical size is the minimum size of a stable nucleus. A nucleus with $r < r^*$ will dissolve back into solution because a decrease in r will decrease the Gibbs free energy, and a nucleus with $r > r^*$ will continue to grow because an increase in r will decrease the

Gibbs free energy. In summary, to form a stable nucleus the particle radius must be greater than r* and the Gibbs free energy must be greater than ΔG^*.[9]

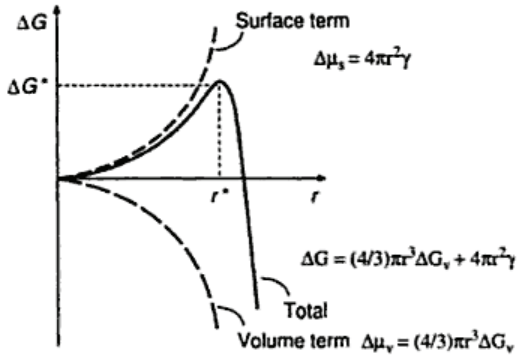

Fig. 1 Change in Gibbs free energy with particle size.
When the nanoparticle reaches a critical cluster size (r^*), growth will continue due to the decrease in Gibbs free energy with continued growth. Below the critical cluster size (r^*), the nanoparticle will dissolve back into solution.

$$\Delta G^* = \frac{16\pi\gamma}{(3\Delta G_v)^2} \tag{5}$$

$$r^* = -\frac{2\gamma}{\Delta G_v}. \tag{6}$$

In heterogeneous nucleation, an existing surface greatly decreases the surface energy per unit area (γ) required for nucleation. Consequently, the activation energy barrier for nucleation to occur (ΔG^*) is also decreased.[10] For this reason, heterogeneous nucleation is more likely to occur than homogeneous nucleation.

It is often desirable to reduce r^* in order to decrease the final crystal size. There are many ways to decrease r^*. The first way is to reduce ΔG^* by increasing ΔG_v and decreasing γ according to equation (5). One way to increase ΔG_v is to increase supersaturation. Since γ can be altered by solvents, additives, and impurities in the

crystal structure, changing any of the above may decrease γ. Temperature also affects γ as well as supersaturation. Fig. 2 shows that temperature directly affects ΔG^* and r^*. As

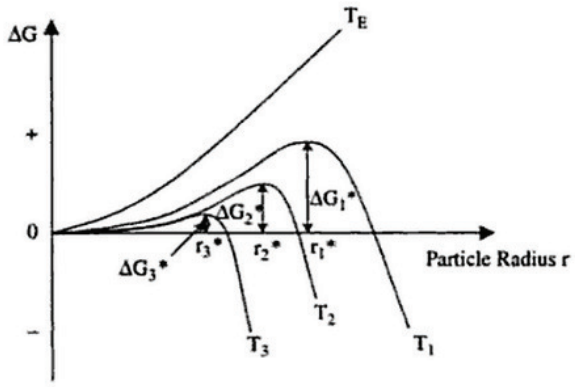

Fig. 2 Influence of temperature on ΔG^* and r^*.
As temperature increases, ΔG^* and r^* increases. In this figure, $T_E > T_1 > T_2 > T_3$, and T_E is the equilibrium temperature.

temperature increases, ΔG^* and r^* increases. Moreover, one can increase the rate of nucleation to decrease r^*. The rate of nucleation is

$$R_N = \left\{\frac{C_o kT}{3\pi\lambda^3\eta}\right\} e^{\left(-\frac{\Delta G^*}{kT}\right)} \tag{7}$$

where c_o is the initial solute concentration and η is the viscosity. This equation indicates that high initial concentration, low viscosity, and low critical energy will increase the number of nuclei formed. The greater the number of nuclei formed, the smaller the size of the equilibrium crystal.[9]

The dependence of crystal nucleation on solute concentration is shown in the La Mer plot (Fig. 3). When solute concentration increases above a critical solute

concentration (C_R), that corresponds to ΔG*, nucleation occur. After the solute concentration decreases below (C_R), the crystal will grow until $S < 1$.[11]

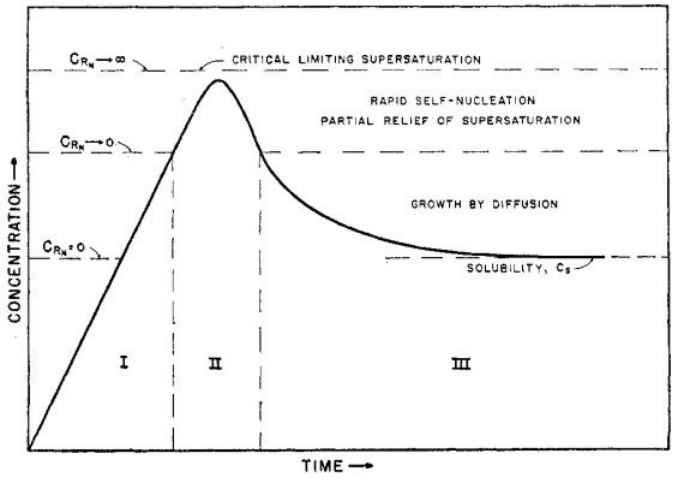

Fig. 3 La Mer plot.
When the solute concentration is above the critical concentration (C_R), nucleation will begin. Crystal growth occurs when solute concentration is between the solubility concentration and C_R.

1.4 Crystal Growth

After a stable nucleus is formed, the crystal will begin to grow. From the thermodynamic perspective, the equilibrium crystal morphology is dictated by the minimization of the surface free energy according to Wulff's rule.[12] Surfaces with large surface energies will grow rapidly, have smaller surface area, or disappear altogether while surfaces with small surface energies will grow slowly and have larger surface area in the final structure. The surface tension (γ) can be approximated by

$$\gamma = \frac{\Delta E_{vap}}{2N_A A_{mol}} \tag{8}$$

where ΔE_{vap} is the evaporation energy, N_A is the Avogadro's number, and A_{mol} is the molecule cross section.[13] Addition of organic or inorganic additives which adsorb onto crystal faces decreases γ by

$$\Delta\gamma = \frac{\Delta E_{ads}}{N_A A_{mol}} \quad (9)$$

where ΔE_{ads} is the molar free energy of adsorption.[6] Consequently, the preferential adsorption of additives to certain faces is a method to alter the equilibrium crystal morphology. However, if additives adsorb indiscriminately onto all crystal surfaces, the crystal growth rate will be reduced resulting in smaller particles. This is because the adsorbed additives act as a stabilizer for the nanoparticles.[14]

Different types of growth also affect the crystal size distribution. Growth occurs in four steps. First, there is the production of growth species. Second, growth species diffuse from the bulk to the growth surface. Third, the growth species adsorbs onto the surface. Lastly, there is an irreversible addition of the growth species to the surface. These four steps can be generalized into two categories - diffusion and growth. Diffusion includes steps one through three, and growth is step four. Growth can be controlled by diffusion or surface processes; these two types of growth results in different crystal size distributions. Growth controlled by surface process can occur in two ways – mononuclear or poly-nuclear. For mononuclear growth, the growth species adds layer by layer; only when one surface layer is complete will the next layer be added. This occurs when there is enough time for the growth species to move around on the surface. In poly-nuclear growth, succeeding layers are created before the preceding layers are

completed. This is caused by a high growth species concentration at the surface driving rapid incorporation of growth species. The change in radius for each type of growth is shown in Fig. 4. Growth controlled by diffusion is the best method to produce monodisperse crystals.[9]

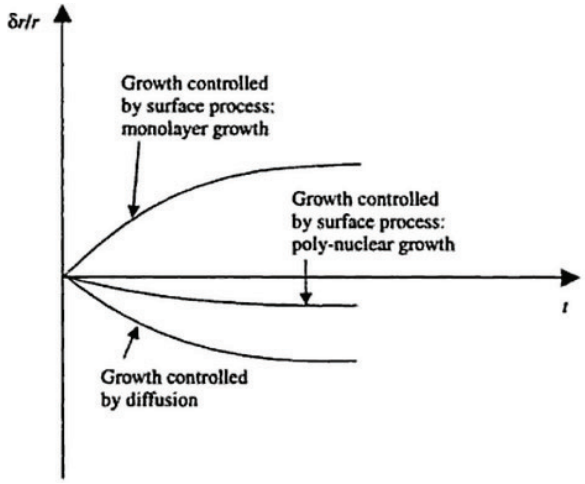

Fig. 4. Influence of growth control on nanoparticle size dispersity.
Growth controlled by diffusion is the best way to produce monodisperse nanoparticles since the difference in radius decreases with increase in time. Growth controlled by surface process will result in polydisperse nanoparticles.

1.5 Hollow Nanocrystals

There has been increased effort in finding methods for producing hollow nanostructures because of their potential impact in the fields of catalysis,[15] separation processes,[16] drug delivery,[17] and energy storage and conversion devices.[18] Generally, hollow nanostructures are prepared by hard, soft, or auto templating.

1.5.1 Hard Templating

Hard templating usually involves four major steps: (1) preparation of hard templates; (2) functionalization or modification of the template surface to achieve favorable surface properties; (3) coating the templates with desired materials or their precursors using various approaches, possibly with post-treatment to form compact shells; and (4) selective removal of the templates to obtain hollow structures.[19] The most commonly employed hard templates are silica particles and polymer latex colloids. Other colloidal systems, such as carbon nanospheres, metal, and metal oxide nanoparticles, have also been used as hard templates for the preparation of hollow nanostructures. The two most common shell-forming strategies for such templates are layer-by-layer assembly and chemical deposition.

Combining layer-by-layer with colloidal templating, Caruso *et al.*[20] pioneered the preparation of hollow inorganic silica and hybrid capsules through electrostatic assembly of negatively charged silica nanoparticles and positively charged polymer. Aside from various polymer capsules,[21] the LBL technique has also been extensively applied to prepare hollow structures of a wide range of inorganic and composite materials,[22] including zeolite/SiO_2,[23] TiO_2,[24] SnO_2,[25] Au,[26] Fe_3O_4,[21] carbon nanotubes (CNTs),[27] etc. However, the LBL method suffers from three key drawbacks. First, the LBL method is difficult to use for the preparation of smaller hollow structures <200 nm. Second, the LBL assembly procedure becomes quite tedious when many layers are required. Third, inorganic and hybrid hollow structures prepared with this method generally lack the mechanical robustness of particles prepared using other approaches. In addition,

prepared polymer capsules are stable only when kept in solution and tend to collapse irreversibly upon drying.

Chemical deposition is another common shell-forming strategy. It involves the precipitation of the shell materials or precursors on the template through various chemical interactions with the template. The deposition process is typically followed by a post-treatment step (usually calcination) to obtain compact shells. Hollow spheres from various materials have been synthesized by chemical deposition. For example, ZnS was deposited on both silica and PS templates under acidic conditions with zinc nitrate and thioacetamide as precursors.[28] Braun and co-workers used a double templating route to obtain ZnS hollow spheres with ordered mesoporous shells, where a lyotropic liquid crystal templates ZnS shell formation on the surface of a silica or polystyrene template.[29] Bimetallic Au/Pt hollow spheres have been prepared by chemical reduction/precipitation of Pt on Au-seeded silica templates followed by the removal of the silica in HF solution.[30]

1.5.2 Soft Templating

While hard and soft templating essentially have the same preparation steps, soft templating makes use of liquid or gaseous particles instead of solid particles as a template. When two immiscible liquids are mixed together by mechanical agitation, liquid droplets of one phase can be dispersed in the other continuous phase, forming an emulsion. In general, emulsions are thermodynamically unstable. Therefore, surfactants or amphiphilic polymers, which self-assemble at the interface between the droplets and the continuous phase, are required to increase kinetic stability.[31] Oil-in-water (O/W) or

water-in-oil (W/O) emulsions are most commonly employed. It should be noted that emulsion polymerization, in which the droplets act as microreactors, has long been used to synthesize solid and hollow polymer spheres.[32] Analogously, the basic idea here is to deposit the shell materials exclusively around the interface between the emulsion droplets and the continuous phase. The precursor shell material can initially exist in either the continuous phase, the droplets, or both phases, depending on the chemistry chosen.

Various examples of emulsion templating have been demonstrated. For instance, Feldmann and co-worker synthesized γ-AlO(OH) hollow nanospheres through hydrolysis of Al(*sec*-$OC_4H_9)_3$ via a W/O (n-dodecane) emulsion templating route, which utilized CTAB as a stabilizer.[33] This strategy gave rise to quite uniform and non-agglomerated γ-AlO(OH) hollow nanospheres with a size of 30 nm. Solders *et al.*[34] synthesized monodisperse silica hollow particles (spheres, capsules, balloons) by templating against low-molecular-weight polydimethylsiloxane (PDMS) silicone O/W emulsion droplets with diameters in the range of 0.6–2 μm. Wang *et al.*[35] synthesized hollow Ag spheres using the phase-transformable emulsions composed of natural beeswax as templates.

The majority of research using gaseous template involve the use of in situ generated gas bubbles. ZnSe hollow spheres have been synthesized under hydrothermal conditions with hydrazine as the reducing agent, in which the resultant N_2 gas bubbles were proposed to play the role of soft templates.[36] Han *et al.*[37] prepared $CaCO_3$ hollow spheres by blowing a mixed gas (CO_2 and N_2) into a solution of $CaCl_2$ and ammonia.

Xie and co-workers synthesized hollow spheres of Co_2P and VOOH by templating against gas bubbles of PH_3 and CH_4,[38] and N_2,[39] respectively.

The two main advantages of soft templating over hard templating are as follows. First, key applications of hollow structures, such as drug and therapeutic delivery, require facile access to the hollow interior space. With the hard templates, refilling the hollow interior with functional species or in situ encapsulation of guest molecules during formation of the shells, though possible, is very challenging. This difficulty can be overcome by soft templating. Second, hard templates suffer from the inherent difficulty of achieving high product yields from the multistep synthetic process and the lack of structural robustness of the shells upon template removal. Because soft templating involves gases and liquids as templates, their removal does not give rise to any significant mechanical stress on the hollow structures, and sometimes there is no need for removal of the template. Among the shortcomings of soft templating are that it predominantly allows the formation of spherical particles because it is only possible to form gaseous bubbles and liquid emulsion templates. In addition, because it is difficult to achieve monodisperse gas bubbles and emulsions,[40] the hollow structures built on these soft templates tend to yield broad size distributions.

1.5.3 Sacrificial Templating

The key feature of sacrificial templating is that the template itself, or its intermediate, is involved as a reactant in the synthetic process of the shell material. Similar to hard templates, sacrificial templates directly determine the shape and approximate cavity size of the resultant hollow structures, but the template

simultaneously plays the role of a structure-directing scaffold and precursor for the shell.[18] As a result, the sacrificial template is consumed partially or completely during the shell-forming process. In this regard, sacrificial template synthesis is inherently advantageous because, in general, it requires no additional surface functionalization and shell formation is guaranteed by chemical reaction. The process is therefore typically more efficient, especially when the sacrificial template is completely consumed during the reaction. The Kirkendall effect and galvanic replacement have been identified as the two most common strategies of sacrificial templating.

The Kirkendall effect, as originally conceived, provides a mechanism for void formation near interfaces due to different inter-diffusion rates in a bulk diffusion couple.[15] The net flow of mass in one direction is balanced by a flux of vacancies, which may condense into voids, preferably around the interface. When applied to spherical particles on the nanoscale, the phenomenon becomes more complicated owing to the dominant roles of curvature and surface energetics.[41] It was first applied by Yin *et al.*[15] to explain the formation of hollow compound nanocrystals of cobalt oxide and chalcogenides about 10–20 nm in size.

The synthesis of hollow nanoparticles based on the Kirkendall process usually involves metal nanocrystals as the core. Gao *et al.*,[42] for example, demonstrated the formation of wires of hollow nanocrystals of cobalt chalcogenides, which were produced by reacting selenium, sulfur, or tellurium with a preassembled 1D necklace-like structure of 20 nm Co nanocrystals. The assembly of Co nanocrystals is induced by the strong magnetic dipoles associated with large Co nanocrystals (20 nm). Such assembly is not

observed for 6 nm Co nanocrystals owing to weaker dipole interaction. Chiang *et al.*[43] recently prepared Ni_2P and Co_2P hollow nanoparticles by a one-pot solution reaction under carefully controlled conditions. The process involves the reaction of first-formed metal nanocrystals with trioctylphosphine (P source). Tan *et al.* reported the formation of hollow Ag_2Se,[44] in which 50-nm spherical Ag nanocrystals were reacted with Se generated from the photo-dissociation of CSe_2 on the surface.

Another type of sacrificial template strategy is galvanic replacement, which have been widely employed for the general preparation of metal hollow nanostructures. In a typical reaction, the salt of a more noble metal (N) is reduced with preformed nanocrystals of a less noble metal (M), resulting in the deposition of N on the surface of M. Upon complete consumption of metal M, hollow structures of metal N can be obtained under controlled conditions. The shape and cavity size of the derived hollow structure are then determined largely by the sacrificial nanocrystals of M.

Xia and coworkers, as well as other research groups, have prepared various metal (Au, Pt, Pd) hollow nanostructures in both aqueous and organic solutions through galvanic replacement reactions with Ag nanocrystals of sizes ranging from <10 nm to several hundred nanometers.[45] The Ag nanocrystals in a wide range of sizes and shapes are synthesized by the versatile polyol process in the presence of a capping reagent such as polyvinyl propylene. In this process, ethylene glycol serves as both a reducing agent and a solvent. Cobalt nanocrystals have also been extensively used as sacrificial templates for the preparation of noble-metal hollow particles through galvanic replacement reactions.[46] Liang *et al.* have prepared hollow nanospheres of Pt,[47] Au,[48]

and bimetallic AuPt,[49] using Co nanoparticles as sacrificial templates and citrate as a capping agent. The Pt hollow nanospheres, consisting of 2-nm Pt nanoparticles, appeared to be largely porous and rough owing to their relatively small overall size of about 24 nm. Depending on the concentration of citrate, either 1D tube-like or discrete hollow nanospheres of AuPt were obtained.

1.6 Auto-templating Assembly of $CaCO_3$-Chitosan Nanoboxes and Nanoframes

Current templating methods have proven very effective and versatile for synthesizing a wide array of hollow structures. However, disadvantages related to high cost and tedious synthetic procedures have impeded the scaling up of many of these methods for large-scale applications. There are some disadvantages to the aforementioned methods. First of all, many of the processes use heavy or noble metals such as Au, Pt, Pd, and Co which are costly. Secondly, hard and soft templating often require calcination at elevated temperatures for template removal.[50] Thirdly, some processes require chemical etching to remove the core. This often requires the use dangerous chemicals which creates hazardous wastes.[51] To realize the use of hollow nanostructures in technological applications, there is a need to develop simpler, more efficient synthesis strategies for producing contamination-free hollow nanostructures using cost-effective materials and environmentally friendly processes on a large scale.

In this research project a new auto templating method for assembling hollow $CaCO_3$-chitosan hybrid nanoboxes and nanoframes in an ionic liquid medium with core removal via dialysis is developed. This method is economical; requires only ambient conditions; and does not produce hazardous wastes. The method of forming hollowing

$CaCO_3$-chitosan nanoboxes and nanoframes was conceived from the fact that biopolymer additives and solvents affect crystal morphology as discussed in the previous sections. Consequently, it was hypothesized that using a new type of solvent called ionic liquids and adding biopolymer chitosan would alter the morphology of $CaCO_3$.

$CaCO_3$ is a natural substance that is commonly found in rocks, eggshells, pearls, and marine animal shells. Derivatives of $CaCO_3$ are used as soil additives, building materials, dietary supplements, and plastics filler. There are many reasons for studying $CaCO_3$. It is inexpensive, highly available, biocompatible, and biodegradable. In addition, $CaCO_3$ has potential for use as a cancer drug carrier.[52]

Chitosan is a polysaccharide made of glucosamine and n-acetylglucosamine units linked by 1 to 4 glycosidic bonds. It is produced by the deacetylation of chitin, which is a component of fungi cell walls and anthropod exoskeleton. Chitosan has been used in bio-related applications due to its hypoallergenic and antibacterial properties. Bandages with chitosan added to improve blood clotting are now used in the battlefields.[53] Within the field of agriculture, chitosan is used as a biopesticide.[54]

Ionic liquids (ILs) are a group of salts that have melting points below 100 °C. Consequently, ILs exist in the liquid state at room temperature. ILs have extremely low vapor pressure compared to traditional volatile solvents; this characteristic qualifies them to be categorized as green solvents. Moreover, particular synthesis and assembly needs can be met by adjustments in the intermolecular and inter-ionic interactions present in the IL solvents.[55] This property allows for the control of nanomaterial shape and morphologies to produce unique nanostructures in an environmentally friendly

manner. In addition, ILs can dissolve biomaterials such as cellulose,[56] chitosan,[57] chitin,[57] and silk[58] which are typically difficult to dissolve in aqueous solutions. This property can be used to incorporate macromolecules into inorganic structures forming a hybrid organic-inorganic material. There are, however, disadvantages to using ionic liquids. It has been recently determined that ILs are toxic and non-biodegradable.[59] Nevertheless, more research on IL properties will result in the improvement of ILs that are designed to be more environmentally friendly.

Instead of using calcination or other harsh chemical means to remove nanostructure cores, dialysis was used in this method. Core removal by dialysis is possible when there is a concentration gradient and solubility difference of components. It has been shown that a polymer concentration gradient may be produced in the formation of hybrid organic-inorganic nanostructures from a solution of mixtures.[60, 61] If the components have different solubility behaviors in a specific solvent, a concentration gradient within a multi-component material can lead to a selective solubility gradient in the material. This in turn may cause the selective removal of one component leading to the formation of a cavity.

2. EXPERIMENTAL TECHNIQUES AND METHODS

2.1 Experimental Techniques

Various material characterization equipment were used to analyze the hollow composites formed in this research project. Specifically, the transmission electron microscope, scanning electron microscope, Fourier transform infrared spectroscopy, and thermal gravimetric analysis were used. The following sections will give a brief description of how each equipment works.

2.1.1 Transmission Electron Microscopy (TEM)

The transmission electron microscope (TEM) is similar to the light microscope in many ways. Instead of using light, the TEM uses a stream of electrons, and instead of using traditional glass or quartz lenses, the TEM uses electromagnetic lenses to magnify the image. The transmission electron microscope is made up of three systems – illuminating, imaging, and specimen manipulation. The illuminating system is composed of the electron gun and condenser lenses. First, a stream of electrons is generated by the electron gun, and the electrons pass through the specimen. The brightness of a particular specimen area is proportional to the amount of electrons transmitted. The condenser lenses regulate the quantity of electrons transmitting through the specimen. Objective, intermediate, and projector lenses are part of the imaging system which form, focus, and magnify the images. Finally, the specimen manipulation system, which includes the specimen stage and holders, are used to orient the specimen for imaging. Modern TEMs are able to magnify images up to 1 million times with a resolution of 0.1 nm. Images generated are 2-D.[62] However, there are some disadvantages to using the TEM. First of

all the sample must be of low density so electrons may pass through it. This means that samples must be thinly sliced. Large specimens must be embedded in resin or frozen and then sectioned. This pre-treatment may alter the specimen. Secondly, the specimen is subject to high vacuum during imaging. This means that the specimen cannot be alive. In other words, it is impossible to observe living specimens *in vivo*.[63]

2.1.2 Scanning Electron Microscopy (SEM)

The scanning electron microscope operates with a lens system which generates a focused spot of electrons, about 2-3 nm in diameter, that is scanned over a specimen surface coated with a thin layer (~ 3-4 nm) of conductive material. SEM can magnify images up to 100,000 times with a resolution of 2.5 nm.[63] As the electrons scan the surface, different types of electrons are released including secondary, backscattered, and transmitted electrons. Backscattered electrons are those that enter the specimen and leave in the direction it came from without affecting the electrons in the electron shell. Secondary electrons are generated during inelastic collision whereby an electron from the beam knocks out an electron from the inner shell. Since secondary electrons have low energy and have a very slight negative charge, they may be collected by a detector with a positive charge to generate a 3-D image. The brightness of each image pixel is proportional to the electron count in a specific region.[62] The disadvantages of using the SEM are similar to those of the TEM. Firstly, the specimen must be stable in high vacuum. This means that the specimens have to be dried and fixed or frozen. In addition, the specimen must reflect enough secondary electron and emit enough secondary back scattered electrons. To meet these requirements, biological samples need to be coated

with a thin layer (~3-4 nm) of conductive material.[63] Usually, gold or platinum is used to coat the specimen.

2.1.3 X-ray Diffraction

Two different methods of X-ray diffraction were used in this research. The first method is X-ray powder diffraction. In X-ray powder diffraction, X-ray is generated by high speed electrons impacting a metal target generating X-rays of a certain wavelength (dependent on the target metal used). The stream of X-rays hits the specimen at an angle θ, and if Bragg's Law is satisfied, constructive X-rays will be reflected at the same angle θ (Fig. 5).[64] Bragg's law is expressed as

$$n\lambda = 2d_{hkl}sin\theta \tag{10}$$

where n is an integer; λ is the wavelength of incident radiation; d_{hkl} is the distance between lattice planes; and θ is the X-ray incident angle. In a typical experimental setup,

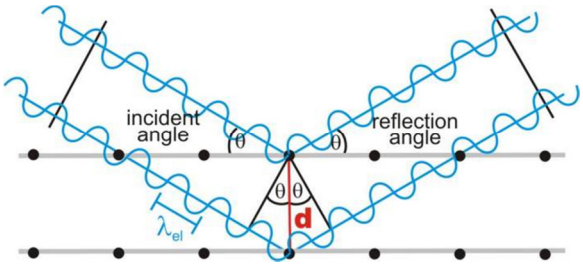

Fig. 5 Diagram of Bragg's law.
Diagram of crystal lattice showing the geometric proof of Bragg's law.

the sample is tilted and the angle of reflected beam is collected. From this data, the lattice planes (Miller's indices) may be calculated using Bragg's Law if the crystal structure (cubic, tetragonal, hexagonal, etc.) is known.[65]

The second method is the single crystal X-ray diffraction. Single crystal X-ray diffraction is based upon the Laune equations:

$$a(cos\psi_1 - cos\varphi_1) = h\lambda \quad (11)$$

$$b(cos\psi_2 - cos\varphi_2) = k\lambda \quad (12)$$

$$c(cos\psi_3 - cos\varphi_3) = l\lambda \quad (13)$$

where a, b, and c are the dimensions of the units cell; ψ and φ are the incident and reflected angle; and h, k, and l are the Miller's indices. Diffraction occurs only when all three Laue equations are satisfied.[65] Using TEM, electrons of various wavelengths pass through a selected area, and the diffraction pattern is collected on a film placed perpendicular to the incident beam. The diffraction pattern is composed of a bright spot in the center surrounded by other less bright spots. The central spot is caused by the non-diffracted rays while the surrounding spots are diffracted rays. Each spot represents a plane. The distance of each spot from the central spot is inversely proportional to the lattice spacing.[62] The diffraction pattern collected is actually a projection onto reciprocal space. Once again, knowing the crystal unit lattice parameters, the Miller's indices per diffraction spot may be calculated by converting reciprocal space into real space.[66]

2.1.4 Electron Tomography

Traditionally, TEM can only produce 2-D images. However, there is a way to produce 3-D images using the TEM. Electron tomography is the reconstruction of 3-D images using TEM projections. This method involves tilting the specimen at a set increment, acquiring images of the specimen at various angles with TEM, and using a computer software to reconstruct a 3-D image. The images are reconstructed by performing a Fourier summation over the projections.[67]

2.1.5 Fourier Transform Infrared Spectroscopy (FTIR)

Fourier transform infrared spectroscopy uses electromagnetic spectrum in the range between 10 and 12,800 cm^{-1} to determine quantitative and qualitative information on a chemical substance. IR photons have the same order of magnitude as the energy difference between molecular vibrational states. Thus, transitions between different vibrational states may be caused by IR radiation. The changes in vibrational states may cause adsorption, emission, or reflection of photons. The difference between impinging IR radiation and the transmitted radiation is used to identify the chemical bonds in the tested substance.[68]

2.1.6 Thermal Gravimetric Analysis (TGA)

Thermal gravimetric analysis is the measurement of sample mass as a function of temperature. A sharp decrease in mass at a certain temperature will occur upon chemical decomposition or boiling. By tracking the change in mass one can determine the mass percentage of different components within a compound if the boiling or decomposition point of each component is known. First, the sample is placed in a sample holder with a

temperature sensor. Then the temperature is raised linearly and the mass of the sample is recorded.[69]

2.2 Experimental Methods

The nanosynthesis of hollow hybrid nanoboxes and nanoframes involve two critical steps: (1) bio-inspired nano-precipitation of inorganic-organic hybrid nanocomposite using ionic liquids as the processing medium and (2) removal of the nano-composite core by a concentration and solubility gradient.

2.2.1 Experimental Procedures

For the synthesis of $CaCO_3$-chitosan nanostructures, calcium chloride dihydrate (99+%), 1-butyl-3-methylimidazolium chloride (≥ 98%), medium molecular weight chitosan, and sodium carbonate (≥ 99%) were purchased from Sigma Aldrich. All chemicals were used as received. 4.01 g [BMIM][Cl], 0.029 g $CaCl_2 \cdot 2H_2O$, and 0.02 g chitosan were put inside a vial and melted at 100°C. After the [BMIM][Cl] dissolved, the mixture was gently stirred until all the solid chitosan was dissolved. Next, 0.2 mL of 1M Na_2CO_3 solution was dispensed into the vial. The solution was sonicated for 30 s with a sonication probe (Misonix XL-2000) at a temperature of 100°C. Lastly, the sample was dialyzed using dialysis membrane (Spectrum Laboratories MWCO: 12,000 - 14,000 daltons) for 72 hours.

2.2.2 Analytical Methods

Transmission electron microscope (FEI Tecnai G2 F20 FE-TEM) and scanning electron microscope (JEOL JSM-7500F) were used to image the nanostructures. For scanning electron microscopy (SEM), samples were coated with 3 nm of Pt/Pd. FTIR

spectroscopy was performed to determine chemical bonding within the sample (Bruker Alpha-P). The crystal structure was analyzed using powder X-ray diffraction (Bruker-AXS D8 Advanced Bragg-Brentano). Samples for X-ray diffraction were filtered, dried overnight, and powderized with mortar and pestle. Then the samples were scanned through a 2θ range of 20 to 70°. A Cu anode was used with $\lambda = 1.54$ Å. The voltage and current were set to 40 kV and 40 mA, respectively. The scan rate was 1°/min, and the step size was 0.015°. Single crystal diffraction pattern and HRTEM image were obtained using transmission electron microscope (JEOL JEM-2010). Thermal gravimetric analysis was performed using TGA Q50. After dialysis was completed, the samples were filtered, dried overnight, and powderized. Samples were scanned from 25 to 1000˚C at a rate of 15˚C/min.

3. RESULTS AND DISCUSSION

The 0.5 wt% $CaCO_3$-chitosan hybrid nanostructures were first analyzed with SEM. SEM images showed that the nanostructures assembled by this method produced hollow rhombohedral structures with dimensions of 339 ± 95 x 299 ± 89 nm with shell thickness of about 75 nm. In addition, SEM micrographs of the $CaCO_3$-chitosan sample after 24 hours of dialysis showed that the sample contained 63% solid nanocubes, 34% nanoboxes, and 3% nanoframes. After 72 hours of dialysis, the sample consists of 28% solid nanocubes, 55% nanoboxes, and 17% nanoframes. This result indicated that dialysis directly influenced the number of nanocubes, nanoboxes, and nanoframes. As dialysis time increased, the ratio of nanoframes to nanoboxes increased and the number of solid nanocubes decreased. The effect of dialysis on nanostructure morphology will be discussed later in this section.

Since it was difficult to differentiate between the nanobox and nanoframe morphology through SEM or TEM micrographs, electron tomography was used to generate 3-D reconstructed images to accurately determine the nanostructure morphology. Electron tomography revealed that two different shapes were prepared. The first type shown in Fig. 6a was a $CaCO_3$-chitosan nanobox with one missing face, and the second type shown in Fig. 6b was a $CaCO_3$-chitosan nanoframe with two missing faces. Iso-surface images revealed that both nanoboxes and nanoframes were slightly porous.

X-ray powder diffraction was used to determine the crystal structure of the

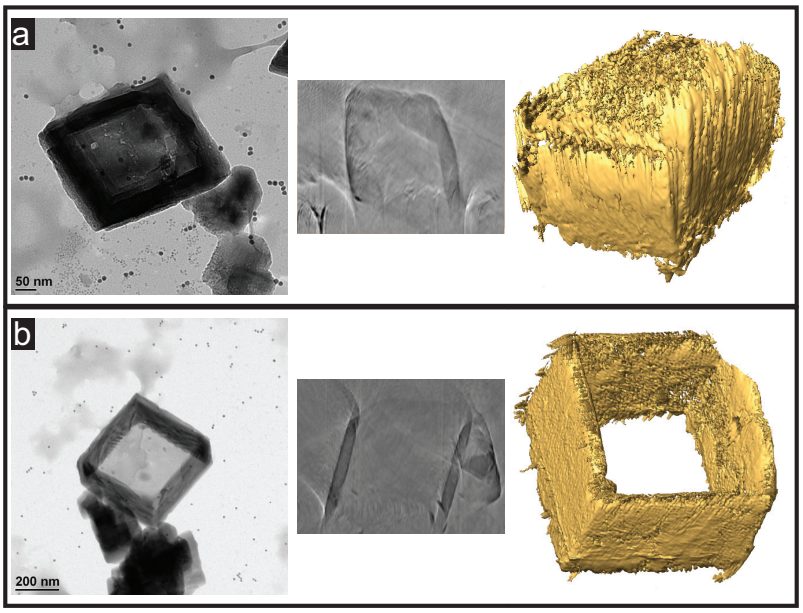

Fig. 6 TEM images of nanobox and nanoframe.
(a) TEM image (left), corresponding cross–sectional image (middle), and iso-surface image (right) of the 3-D reconstructed nanobox structure with one missing face after 24 hours dialysis. (b) TEM image (left), corresponding cross-sectional image (middle), and isosurface image (right) of nanoframe with two missing faces after 72 hours dialysis.

$CaCO_3$-chitosan nanocubes, nanoboxes, and nanoframes. Three samples were analyzed – pure $CaCO_3$ and $CaCO_3$-chitosan nanostructures after 24 and 90 hours dialysis. The $CaCO_3$-chitosan sample after 24 hours of dialysis was nanobox rich, and the $CaCO_3$-chitosan sample after 90 hours of dialysis was nanoframe rich. X-ray diffraction patterns indicated that all three samples (nanocubes, nanoboxes, and nanoframes) were of calcite morphology (Fig. 7). In addition, X-ray powder diffraction of pure $CaCO_3$ nanocrystals prepared in water and in 1-butyl-3-methylimidazolium chloride [BMIM][Cl] as well as the $CaCO_3$-chitosan sample after 72 hours of dialysis using the same experimental conditions were obtained (Fig. 8a). These patterns indicated that all three samples were

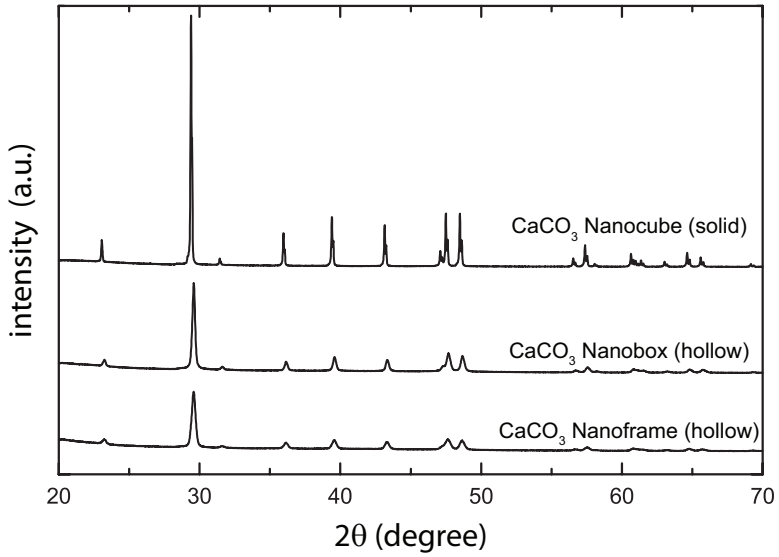

Fig. 7 X-ray powder diffraction pattern of $CaCO_3$-chitosan nanostructures.
Analysis of the diffraction patterns indicates that all $CaCO_3$ nanoparticles including the hybrid $CaCO_3$-chitosan nanoboxes were of calcite morphology.

of calcite morphology. However, the patterns obtained exhibited peak broadening. In this case there may be two possible causes of peak broadening - the introduction of crystal defects due to the intercalation of a polymeric additive[14] or a decrease in nanocrystal size as described by the Scherrer equation.[70] To quantitate the peak broadening, the (113) peak in each pattern was fitted to a Gaussian curve and the full width at half maximum (FWHM) was calculated for each sample (Fig. 8b). The (113) peak of pure calcite prepared in water, pure calcite prepared in [BMIM][Cl], and $CaCO_3$-chitosan hybrid nanostructure had a FWHM of 0.160, 0.244, and 0.274, respectively. This indicated that calcite formed in water had the least degree of crystal strain or formed the most perfect calcite crystal. When the solvent was changed to [BMIM][Cl], the degree of crystal strain increased as evidence by the increased peak broadening. Finally, when chitosan was added, even more crystal strains and pores were introduced.

This finding was consistent with iso-surface images of slightly porous nanoboxes and nanoframes. Similar peak broadening due to stress and porosity were also observed by other researchers. Budrovic *et al.*[71] showed that when stress was applied to nano-crystalline nickel disrupting the crystal lattice, the FWHM of the diffraction peaks increased. McAllister *et al.*[72] observed increased peak broadening with increased corrugation in graphite oxide structures. Additionally, although the same experimental conditions were used for all three samples, the nanocrystals differed in size. The dimensions of the pure $CaCO_3$ in water and [BMIM][Cl] are 4.79 ± 1.70 x 3.94 ± 1.52 μm and 340 ± 14 x 273 ± 116 nm respectively while the $CaCO_3$-chitosan nanostructure had dimensions of 339 ± 95 x 299 ± 89 nm. With the change in solvent from water to [BMIM][Cl], the calcite structures decreased in size but with the addition of chitosan, the nanostructure dimensions stayed about the same.

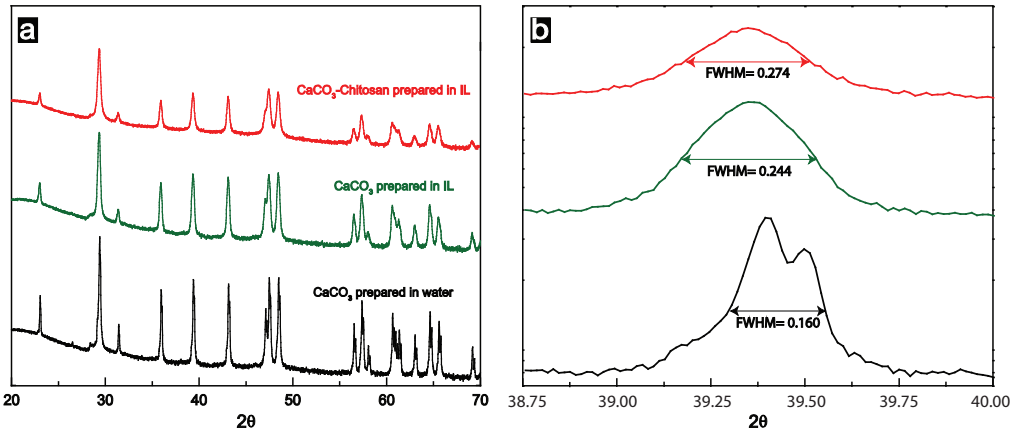

Fig. 8 X-ray powder diffraction patterns with peak broadening.
(a) X-ray powder diffracion pattern of $CaCO_3$-chitosan hybrid nanostructures, pure $CaCO_3$ prepared in [BMIM]Cl, and pure $CaCO_3$ prepared in water. (b) Calculated FWHM showing peak broadening with the change of solvent from water to [BMIM][Cl] and the addition of chitosan.

These results showed that the cation group of [BMIM][Cl] behaved similarly to an organic biopolymer additive by adsorbing onto inorganic $CaCO_3$ nanoparticle surfaces. This was possible through the interaction of the tertiary amine group in $[BMIM]^+$ cation with $CaCO_3$ (Fig. 9).[73] Mann *et al.*[74] showed that $CaCO_3$ crystal

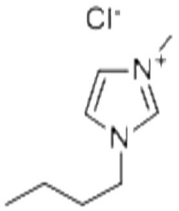

Fig. 9 Chemical structure of [BMIM][Cl].
This figure shows the chemical structure of the ionic liquid [BMIM][Cl]. It is possible that the tertiary amine group of the cation interacts with calcite surface causing intercalation of $[BMIM]^+$ in the calcite crystal lattice.

nucleation on a monolayer of positively charged octadecylamine influenced crystal morphology. Sugihara *et al.*[75] synthesized disk-like vaterite crystals by adding ethylenediamine, diethylenetriamine and other polyamines. In addition, it was shown that cyclic amine additives cause the formation of spindle $CaCO_3$.[76] These studies proved that the amine group does indeed interact with inorganic $CaCO_3$ surfaces thereby influencing its equilibrium morphology. This interaction may explain the decrease in $CaCO_3$ nanocrystal size with the change in solvent from water to [BMIM][Cl]. The addition of low to moderate concentrations of polymeric additives can alter the morphology of crystals by Wulff's rule if polymer adsorption is selective.[12] However, with high concentrations of polymer additives, there would be a quenching in crystal growth due to the steric hindrance preventing the addition of growth element.[14] In this instance, since a large amount of solvent compared to inorganic solute was used, there

was a total coverage of the growing nanoparticle surface, preventing growth. Consequently, the final size decreased.

In addition, as the positive cations of [BMIM][Cl] adsorbed onto $CaCO_3$, it was possible for overgrowth of inorganic crystal to occlude the cationic polymeric additives causing peak broadening. Polymer latexes have shown to behave in this manner with calcite single crystals.[77] In nature, sea urchin skeletons, made of calcite, also have occluded acidic glycoprotein.[78] Berman *et al.*[79] showed in a well-known paper that sea urchin spine with occluded acidic glycoprotein showed increase in FWHM of X-ray diffraction patterns compared to that of pure calcite. Aizenberg *et al.*[80] also showed that the reciprocal of angular spread or degree of alignment decreased with occluded macromolecules. Synthetic calcite had a degree of alignment of 180/° while the Clathrina triradiate spicule had a degree of alignment of 16/°.[81] Based on their research, it was possible that the increased FWHM in the X-ray diffraction pattern when the solvent was changed from water to [BMIM][Cl] be due to the surface attachment and/or intercalation of $[BMIM]^+$ in the calcite structure.

As mentioned previously, with the addition of chitosan, the FWHM increased from 0.244 to 0.274. However, there was not a significant size change from the pure calcite sample made with [BMIM][Cl] solvent. Similar to the $[BMIM]^+$ structure, chitosan has primary amine functional groups (Fig. 10).[82] The amine functional groups have the ability to interaction with calcite nanoparticles.[74-76, 81] Like $[BMIM]^+$ it was possible that chitosan adsorbed onto the surface of the calcite particles inhibiting growth. Since, there was already so much solvent, the added biopolymer chitosan did not

significantly decrease the calcite nanocrystal size because compared to the solvent concentration, the concentration of chitosan may be assumed to be negligible (0.5 wt%). However, it was clear that chitosan must have been occluded into the calcite structure due to the increase in FWHM by reasons given in the previous paragraph. Therefore, the increase in FWHM with the addition of chitosan was due to the adsorption and occlusion of chitosan in the calcite crystal lattice.

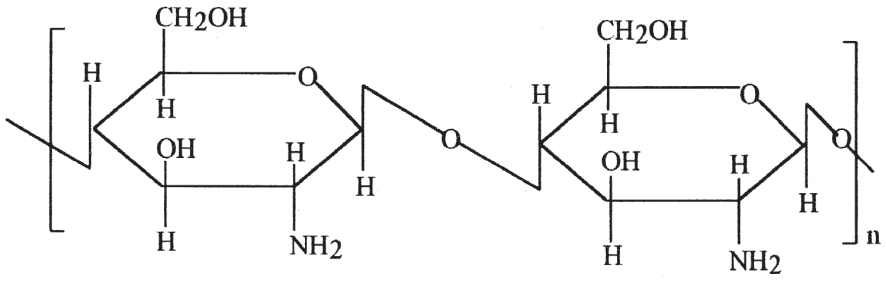

Fig. 10 Chemical structure of chitosan.
The chemical structure of chitosan has primary amine functional groups that allow it to adsorb onto calcite surfaces.

Knowing now that the sample was a calcite-chitosan hybrid, it was desired to find out if it was a single crystal. Selected-area electron diffraction (SAED) and high-resolution TEM (HRTEM) imaging of nanoboxes revealed their single crystal nature. As shown in Fig. 11a, the center nanobox exhibited dark contrast on the frame (due to the thickness) but with a base on either top or bottom side rather than empty area indicated by a little broken area at the lower-right corner (arrow indicated). The SAED from this box base area showed a single crystal pattern (shown in the inset) which was indexed as the [-441] zone axis. The nanobox adjacent to it on the upper-left side also showed a

single-crystal SAED pattern (not shown). The beautiful diffraction pattern (Fig. 11a inset) showed that the calcite-chitosan nanoboxes were single calcite crystals because of the clear separated individual spots. This was similarly shown by Qi *et al.*[83] for single crystal vaterite disks and Goldberg *et al.*[84] for single crystal gallium nitride nanotubes. Whereas diffraction pattern of separated rings were obtained by Yu *et al.*[85] for polycrystalline vaterite. A HRTEM image from the outlined area in Fig. 11a is shown in Fig. 11b. On the nanobox frame, it was not possible to see the lattice fringes due to its thickness, but the lattice fringes were visible in the base area. A Fourier transform (FT) pattern is shown at the top-right corner of Fig. 11b with reflections similar to the SAED pattern in Fig. 10a inset; this confirmed the SAED was from the nanobox base area. A further magnified image is shown at the bottom-right corner of Fig. 11b with crystallographic orientations indicated.

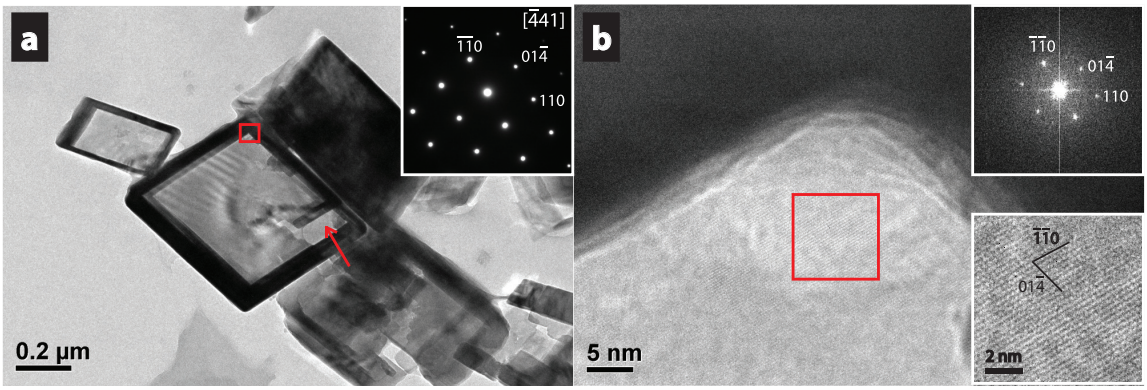

Fig. 11 Selected-area electron diffraction and high-resolution TEM of nanobox.
(a) Representative TEM image showing $CaCO_3$-chitosan nanoboxes with a SAED pattern from the center nanobox. (b) HRTEM image from the outlined area in (a), with a Fourier transform pattern and a further magnified imaged from the outlined area.

To find out the organic and inorganic composition of the calcite-chitosan hybrid nanostructures, TGA was performed on two samples – a nanobox rich sample (24 hours dialysis) and a nanoframe rich sample (90 hours dialysis). 8.15 mg of 24 hours sample and 16.06 mg of 90 hours sample were used in the analysis. TGA revealed that the nanobox rich sample had 38 wt% chitosan while the nanoframe rich sample had 34 wt% chitosan (see Fig. 12). It can be seen in Fig. 12 that chitosan decomposed around 300˚C while calcite decomposed at about 750˚C. Weight loss from 50 to 150˚C was attributed to water loss in the samples. There was about 7 wt% water in both samples. In the nanobox rich sample there was 55 wt% $CaCO_3$ and 38 wt% chitosan; in the nanoframe rich sample there was 59 wt% $CaCO_3$ and 34 wt% chitosan. These results showed that with dialysis more chitosan was removed than calcite due to a concentration gradient within the nanostructures itself.

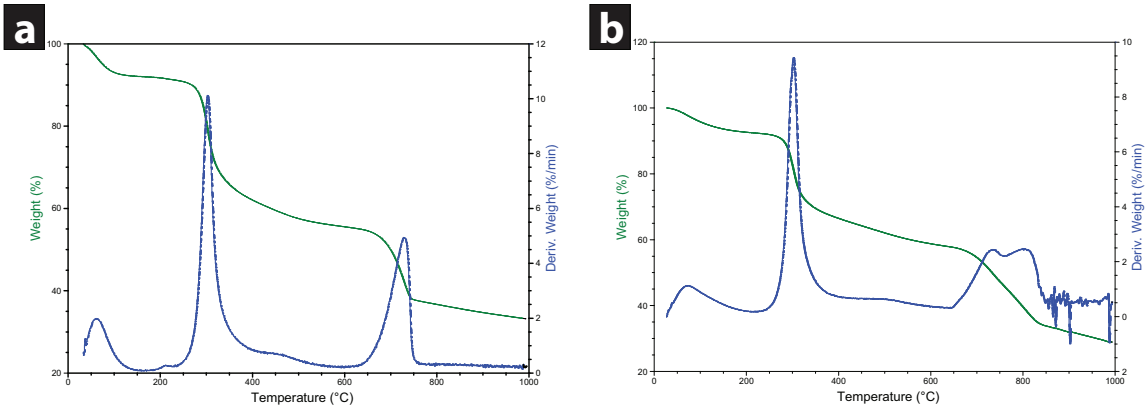

Fig. 12 Thermal gravimetric analysis of nanobox and nanoframe rich sample.
Thermal gravimetric analysis result of $CaCO_3$-chitosan sample after (a) 24 hours and (b) 90 hours of dialysis.

In order to determine whether any chemical bonds were formed between calcite and chitosan, FTIR spectroscopy was performed (Bruker Alpha-P). $CaCO_3$ prepared in water yielded peaks at similar wavelengths to those of $CaCO_3$ prepared in [BMIM][Cl] (Fig. 13a,b). According to published literature, the carbonate ion should generate three FTIR peaks at 706, 874, and 1429-1492 cm^{-1} due to in plane deformation, out of plane deformation, and in plane asymmetric stretching, respectively.[86] This was consistent with the first three peaks observed in Fig. 13a, b. The weak peak at about 1794 cm^{-1} was due to the carbonyl band.[86] In addition, FTIR was also performed on the $CaCO_3$-chitosan hybrid (Fig. 13c). Once again, the 708, 871, 1400 and 1795 cm^{-1} peaks may be attributed to CO_3^{-2}.[86] The peaks from 1000-1200 cm^{-1} may be caused by glycosidic linkage of chitosan. The C=O group in the amide group resulted in a peak at about 1795 cm^{-1}. The peak at 2873 cm^{-1} was due to the CH_2 groups in the pyranose ring. Lastly, the stretching of the NH group caused the weak peak at 3320 cm^{-1}.[87]

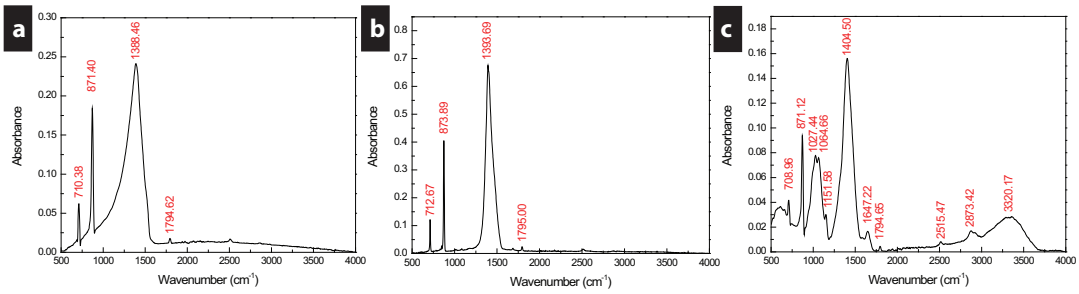

Fig. 13 FTIR spectra of nanostructures.
FTIR spectra of (a) $CaCO_3$ prepared in water, (b) $CaCO_3$ prepared in ionic liquid [BMIM][Cl], and (c) $CaCO_3$-chitosan hybrid prepared in ionic liquid [BMIM][Cl].

When the solvent was changed from water to [BMIM][Cl], a peak shift of ~5 cm^{-1} (1388.45 cm^{-1} peak in the Fig. 13a to 1393.69 cm^{-1} in Fig. 13b) was observed for the

CO_3^{-2} asymmetric in plane stretching peak. As mentioned above in the powder X-ray discussion, this may be attributed to hydrogen bonding of $[BMIM]^+$ to calcite surface. However, since there was no additional peaks indicating the presence of $[BMIM]^+$, the FTIR spectra showed that, at least on the outer surface, $[BMIM]^+$ was not attached to the surface during analysis. Nevertheless, one must consider that it was possible that $[BMIM]^+$ was completely removed from the nanostructure surface by dialysis treatment. Perhaps, $[BMIM]^+$ had more affinity towards water than the carbonate group thereby causing the complete removal of $[BMIM]^+$. On the other hand, a significant peak shift of ~10 cm^{-1} was observed after the addition of chitosan (1393.69 cm^{-1} in Fig. 13b to 1404.56 cm^{-1} in Fig. 13c). This may be caused by the absorption of chitosan to $CaCO_3$ surface by hydrogen bonding. The additional peaks in the FTIR spectra indicate that chitosan was present on the calcite surface. Chitosan was not desorbed from the calcite surface because it was water insoluble; its surface interaction with calcite was favored over its interaction with water.[88] Previous work had also used FTIR peak shift as reason to justify physical adsorption on surfaces via hydrogen bonding. Sun *et al.*,[89] associated a 5 cm^{-1} peak shift of the C=O band to hydrogen bonding between $Au/HS(CH_2)_2COOH$ and $CH_3(CH_2)_{12}COOH$ layers. In addition, a 16 cm^{-1} shift in the C=O band has been attributed to hydrogen bonding.[90]

To further understand the mechanism by which these hollow nanostructures were formed, electron microscopy studies were performed by altering the chitosan to $CaCO_3$ weight ratio, sonication power, temperature, and dialysis time. It should be noted that using the SEM only two dimensions were measured – the “short” and “long.” However,

such comparison with large quantity measurements should still lead to useful insight about the relative sizes of nanostructures.

In the chitosan to $CaCO_3$ weight ratio study, the weight ratio of chitosan to $CaCO_3$ was varied to determine its effect on the size and shape of the nanoparticles. The chitosan to $CaCO_3$ weight ratios studied were 1:1, 1.5:1, and 2:1, where the $CaCO_3$ concentration was 0.5 weight % in [BMIM][Cl] for all mixtures. Fig. 14 shows clearly that as the chitosan to $CaCO_3$ weight ratio increased, the nanostructure size decreased.

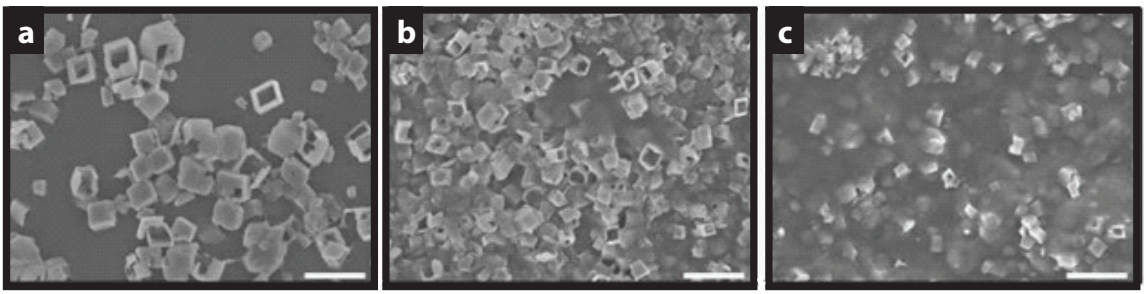

Fig. 14 SEM images of chitosan to $CaCO_3$ weight ratio study.
Hybrid nanostructures obtained with chitosan to $CaCO_3$ weight ratio of (a) 1:1, (b) 1.5:1, and (c) 2:1 showing that nanostructure size decreases with increased chitosan to $CaCO_3$ weight ratio. The scale bar is 1 μm.

The dimensions of the 1:1, 1.5:1, and 2:1 samples are 336 ± 55 nm by 396 ± 65 nm, 245 ± 65 nm by 284 ± 86 nm, and 175 ± 43 nm by 217 ± 58 nm, respectively. One possible reason for this result is that the addition of chitosan increased the rate of nucleation by heterogeneous nucleation. The dissolved chitosan provided a free surface upon which $CaCO_3$ may nucleate. The absorption of chitosan on the $CaCO_3$ surfaces caused a decrease in γ and consequently an increase in the rate of nucleation as indicated in equation (7).[9] Another possibility is that increasing the chitosan concentration increased

the biopolymer surface coverage of the nanostructures thereby decreasing growth due to steric hindrance.[14] The concept of biopolymers inhibiting crystal growth was demonstrated experimentally. Treccani *et al.*[91] experimentally proved that the addition of abalone protein perlwapin deterred the growth of calcium carbonate crystals due to perlwapin binding to step edges preventing growth. In addition, work by Wheeler *et al.*[92] showed that a soluble protein extracted from oyster shell is effective in preventing calcium carbonate growth.

For the sonication power study, the samples were sonicated at 10, 20, and 30 W power for 30 s while all other experimental parameters were kept constant. SEM images of the resulting nanostructures are shown in Fig. 15. The results of size analysis indicated that as sonication power increased, the nanostructure size decreased (Fig. 16). At 10, 20, 30 W power, the dimensions of the nanostructures were 339 ± 95 x 289 ± 44 nm, 291 ± 49 x 274 ± 44 nm, and 259 ± 52 x 255 ± 35 nm, respectively. The inverse relationship between mixing strength and nanostructure size may be explained by equation (7) where the rate of nucleation is indirectly proportional to viscosity. As mixing rate or shear rate increased, the viscosity of the solution decreased. It may be suggested that the chitosan IL polymer solution exhibited shear thinning which is characteristic of polymer solutions.[93] Therefore as the rate of mixing increases, the rate of nucleation increased causing the observed decrease in nanostructure size.

For the temperature study, the experimental temperature was changed from the original 100˚C to 80, 120, 140, and 160˚C. SEM images of the samples produced with different experimental temperatures were taken, and from the SEM images the “short”

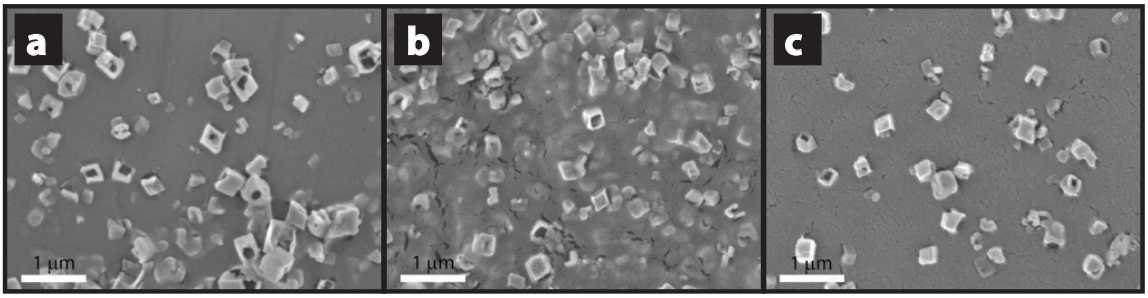

Fig. 15 SEM images of sonication power study.
The results of hybrid nanostructures obtained with **(a)** 10 W, **(b)** 20 W, and **(c)** 30 W sonication power. The images showed that as sonication power increased, nanostructure size decreased.

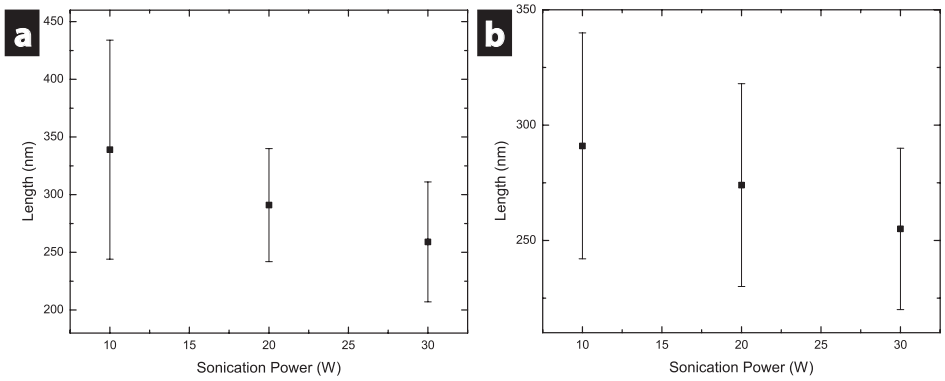

Fig. 16 The effect of sonication power on nanostructure dimensions.
The (a) long and (b) short nanostructure dimension as a function of sonication power. The trend shows that nanostructure size decreased with increase in sonication power.

and "long" lengths of the nanostructures were measured. The nanostructure dimensions of the 80, 120, 140, and 160°C samples were 319 ± 80 x 277 ± 68, 322 ± 77 x 284 ± 65, 327 ± 79 x 281 ± 66 nm, and 350 ± 101 x 310 ± 93, respectively.

From these results it may be concluded that temperature did not have any influence on the equilibrium nanostructure dimension or morphology (Fig. 17). However, it was predicted that nanostructure size should decrease with increased temperature and nucleation rate.[9] In addition, research by Zeller and Wray showed that

temperature directly influences equilibrium $CaCO_3$ morphology. They showed that calcite and vaterite precipitated at 10°C; only calcite precipitated at 23°C; and a mixture of aragonite and calcite were obtained at 52°C.[94] Burton and Walter also showed that at 5°C the rates of calcite and aragonite precipitation were nearly equivalent while at 25 and 37°C aragonite precipitated more rapidly than calcite.[95] However, their experiment was set up so that the crystals aged in a constant temperature bath. This is intrinsically different from the present experimental set up where the crystals aged at room temperature and only the temperature during mixing was changed. A possible explanation for the present result is that shear rate exerted greater influence over nucleation than temperature during mixing. Since the same shear rate was used for all samples, the nanostructure size did not change. Furthermore, since all samples were aged at room temperature, the equilibrium morphology was not altered.

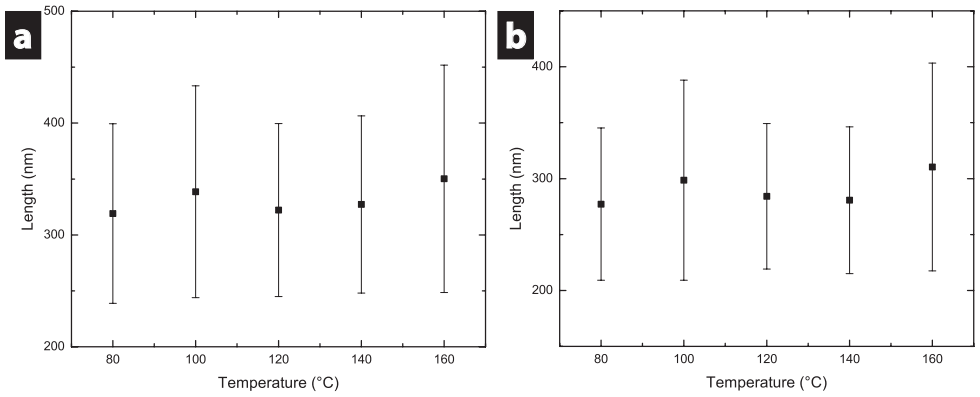

Fig. 17 The effect of temperature on nanostructure dimensions.
The (a) long and (b) short nanostructure dimensions as a function of experimental temperature.

Lastly, the effect of dialysis time on the $CaCO_3$-chitosan morphology was studied. The dialysis times studied were 24, 48, and 72 hours. Before the start of dialysis, rhomobohedral calcite crystals without visible surface defects were obtained (Fig. 18a). After 24 hours of dialysis, structures with mild surface defects were found (Fig. 18b). With increased dialysis for 48 hours, surface defects deepened to become visible cavities on the nanostructure surface (Fig. 18c,d). Finally, after 72 hours of dialysis, hollow nanoframes were formed; some nanoframes were more eroded than others (Fig. 18e,f).

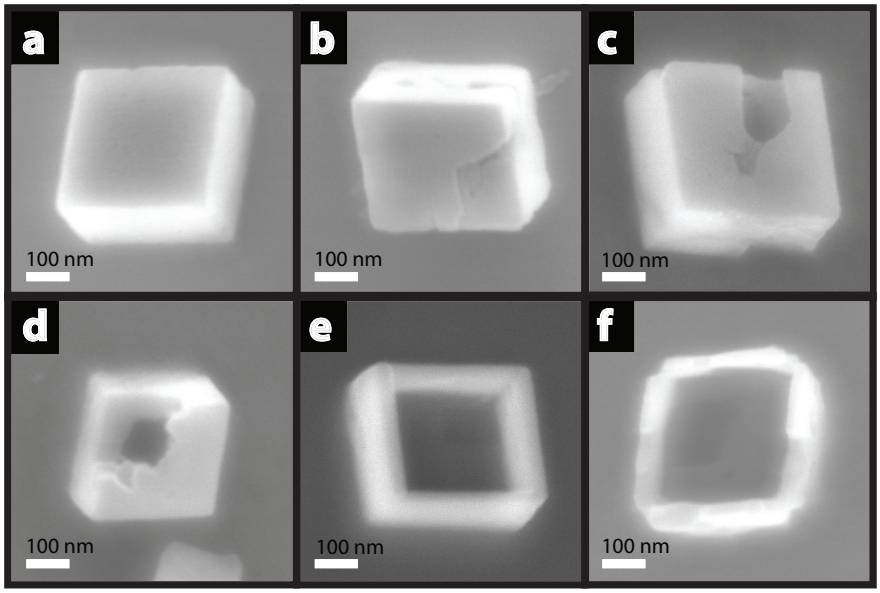

Fig. 18 SEM images of the dialysis time study.
(a) Rhombohedral nanostructures without surface defects are formed before dialysis. (b) After 24 hours of dialysis, nanostructures with visible surface defects are observed. (c) As dialysis progressed for 48 hours, [BMIM][Cl] and chitosan leach out from the surface defects creating shallow cavities. (d) As more and more chitosan leach out, there is increased contact with water and deeper cavities are formed. (e) After 72 hours of dialysis, nanoframes are formed. (f) With further dialysis, the frames show signs of more erosion.

Generally, core removal was by calcination or chemical etching. Chen *et al.*[96] produced hollow silica particles by removing $CaCO_3$ template core through calcination at 700°C followed by chemical etching with HCl. Hollow silica nanotubes were made by removal of calcium carbonate template by calcination at 823K and chemical etching with acetic acid.[97] A novel form of chemical etching was reported by Gao *et al.*[60] who found that using a double hydrophilic block co-polymer with ethylenediamine tetraacetic acid (EDTA) resulted in the formation of calcium carbonate microrings. This chemical etching was caused by a higher concentration of EDTA in the core. As the nanostructures aged, the EDTA etched the core away forming hollow microrings.

Calcination and chemical etching were not employed in this research since neither elevated temperatures nor acidic chemicals were used. However, the SEM micrograph results from the dialysis study indicated that during dialysis an etching process occurred by which the core of the nanostructure was increasingly removed as dialysis time progressed. This etching process may be attributed to the chitosan concentration gradient within the nanostructures. The pairing of the chitosan concentration gradient with selective solubility of chitosan in [BMIM][Cl] over water may be the cause for the selective removal of components and cavity formation.

From the results obtained, one may deduce that during nucleation $CaCO_3$ nanoparticles were stabilized by chitosan and $[BMIM]^+$ adsorption onto their surface. These hybrid nanoparticles were more stable compared to $CaCO_3$ nanoparticles without any chitosan or $[BMIM]^+$ adsorbed onto their surfaces.[14] This concept had been proven by Li and Mann who showed that amorphous calcium carbonate may be stabilized with

surfactants attached to its surface.[98] It had also been shown that polycarboxylate bound to the surface of calcium carbonate nanoparticles acted to stabilize the nanoparticles.[99] The stabilized hybrid nanoparticles had greater probability to collide with one another and aggregate to form larger nanoparticles with chitosan and $[BMIM]^+$ included. As these nanoparticles reach the critical radius, a stable nucleus composed of hybrid nanoparticles and [BMIM][Cl] was formed. As nucleation and growth progressed, the concentration of chitosan in solution decreased. Consequently, as growth progressed a chitosan concentration gradient was produced within the nanostructure where the chitosan concentration decreased from the core to the surface. This mechanism was first described by Gao *et al.*[60] for the formation of $CaCO_3$ microrings. Similarly, Dong *et al.*[61] used this explanation to describe the formation of $CaCO_3$ hollow spheres.

When the sample was dialyzed, first the [BMIM][Cl] solvent surrounding the nanostructures was removed along with the $[BMIM]^+$ adsorbed onto the surface. FTIR analysis confirmed this suggestion. As a result, this automatically introduced a $[BMIM]^+$ chemical potential difference inside and outside the nanostructures that drove $[BMIM]^+$ enclosed within the nanostructures to leave the nanostructure core through surface defects (caused by $[BMIM]^+$ removal) in order to balance the $[BMIM]^+$ chemical potential. The introduction of crystal defects through the removal of [BMIM][Cl] was evident from both the X-ray diffraction and FTIR analysis. Since chitosan was soluble in [BMIM][Cl], as $[BMIM]^+$ was removed from the crystal lattice, chitosan was also carried along. This was consistent with TGA results which showed that the chitosan fraction decreased upon increased dialysis times. Due to the chitosan concentration

gradient within the nanostructure, the core was selectively removed first while the frame stayed intact. The removal of chitosan and $[BMIM]^+$ disrupted $CaCO_3$ bonding causing $CaCO_3$ to disintegrate and leave the core through surface defects. As $[BMIM]^+$ and chitosan were continually removed, small surface defects became larger thereby increasing water-nanostructure surface contact area. Eventually, a small defect became a large cavity forming nanoboxes and eventually nanoframes. Nanostructure erosion continued until water was removed completely. This proposed mechanism is consistent with all the material analysis previously mentioned.

Although preliminary results have been obtained from this research, more improvements are necessary. It should be noted that the nanostructures formed were not uniform in size, and not all nanostructures formed were hollow. Generally, solid nanostructures observed were much smaller than the hollow nanostructures. Firstly, this implied that the nucleation time was too long. At the beginning of nucleation, hybrid nuclei were formed. Towards the end of nucleation, pure calcite nucleated. Secondly, the size distribution indicated that growth was dependent on surface integration rather than diffusion. More uniform size structures may be formed by incorporating diffusion of reactants into the process. Albeck *et al.*[100] first described a method of forming calcium carbonate-glycoprotein structures using diffusion to produce uniform sized crystals. In this method a solution of calcium chloride was put into a dessicator with solid ammonium carbonate. As the ammonium carbonate solid sublimed, calcium carbonate was formed in solution. This method was used by others to make uniform calcium carbonate crystals.[60, 101] However there were disadvantages to using diffusion. First

diffusion slowed down the process. It took 15 days for $CaCO_3$ microrings to be formed using the same method.[60] Moreover, the crystal obtained had dimensions in the micrometer range.[60, 100, 101]

It may be possible that improvements in other directions may improve crystal size uniformity. Future studies on the kinetics of each experimental step are necessary to pin point where nucleation and growth occurs in order to make necessary improvements. Moreover, it is necessary to find a better method to measure the size of the hollow nanostructures. Since these hybrid nanostructures were not able to be analyzed by dynamic light scattering, it was not possible to accurately determine nanostructure size except by measuring the "short" and "long" lengths in SEM images. It would be interesting to study the effect of equilibrium temperature on the hybrid chitosan-$CaCO_3$ morphology since it was kept constant for this research. Lastly, a study on the influence of pH on crystal morphology is necessary.

4. CONCLUSION

In summary, this thesis presents an auto templating method of forming hollow hybrid nanoframes and nanoboxes using an ionic liquid solvent at ambient conditions. The transformation from nanocubes to nanoboxes and nanoframes was attributed to selective core etching during dialysis. By varying the chitosan to $CaCO_3$ weight ratio, it was determined that as chitosan to $CaCO_3$ weight ratio increased, the nanoparticle sizes decreased. In addition, it was shown that increasing the sonication power caused the nanostructure size to decrease. However, changing the mixing temperature in the range of 80 – 160˚C did not affect equilibrium nanostructure size. The dialysis study showed that the nanostructure core was progressively removed. After 72 hours of dialysis, nanoframes were observed with SEM. Based on these results, a mechanism for forming these nanostructures was presented. Using this method, it only took 3 days to make the hollow hybrid nanoframes and nanoboxes. This mechanism has potential to be used to synthesize other types of hollow nanostructures in an environmentally friendly, low cost, and rapid manner.

As for future prospective, these hollow nanoboxes and nanoframes can find a variety of applications in catalysis,[15] separation processes,[16] drug delivery,[17] and energy storage and conversion devices.[18] It is envisioned that these hybrid nanostructures may be used as a drug delivery agent due to the biocompatibility of both $CaCO_3$ and chitosan. More studies on the kinetics of shell decomposition may allow the design of nanostructures capable of releasing therapeutics at controlled times. Also, control over the porosity of these nanoframes could allow them to be used for catalysis and

separation processes. Lastly, it is possible that the nanoframes maybe coated with TiO_2 for use in solar cells.

REFERENCES

1 J. Brady and F. Sense, *Chemistry: The Study of Matter and Its Changes*, New Jersey: Wiley, 2004, 559-560.

2 G.F. Arkenbout, *Melt Crystallization Technology*. Pennsylvania: Technomic Publication, 1995, 3-4.

3 (a) Y. Wu, J. Xiang, C. Yang, W. Lu and C. Lieber, *Nature*, 2004, **430**, 61-65; (b) L.C. Chen, C.K. Chen, S.L. Wei, D.M. Bhusari, K.H. Chen, Y.F. Chen, Y.C. Jong and Y.S. Huang, *Appl. Phys. Lett.*, 1998, **72,** 2463.

4 (a) T. Ishihara, H. Matsuda and Y. TAkita, *J. Am. Chem. Soc.*, 1994, **116**, 3801-3803; (b) K. Hayashi, S. Matsuishi, T. Kamiya, M. Hirano and H. Hosono, *Nature*, 2002, **419**, 462-465.

5 (a) S. Sano, *Am. J. Clin. Nutr.*, 2009, **90**, 7285-7325; (b) S. Ranganathan, S. Sundaresan, I. Ragharendra and S. Kalyani, *Asia Pacific J. Clin. Nutr.*, 1997, **6**, 92-94.

6 (a) N. Blagden, M. de Matas, P.T. Gavan and P. York, *Adv. Drug Deliver. Rev.*, 2007, **59**, 617-630; (b) Z.J. Li and D. Grant, *J. Pharm. Sci.,* 1997, **86**, 1073-1078.

7 J.S. Wey and P.H. Karpinski, *Handbook of Industrial Crystallization*, Ed. A. Myerson, Boston: Butterworth-Heinemann, 2001, 231.

8 P. Barrett, B. Smith, J. Worlitschek, V. Bracken, B. O'Sullivan and D. O'Grady, *Org. Process Res. Dev*., 2005, **9**, 348–355.

9 G. Cao, *Nanostrutures & Nanomaterials*. London: Imperial College Press, 2004, 53-62.

10 S. Mann, *Biomineralization Principles and Concepts in Bioinorganic Materials Chemistry.* New York: Oxford University Press, 2001, 43.

11 V.K. La Mer, *Ind. Eng. Chem.*, 1952, **44**, 1270-1277.

12 G. Wulff, *Z. Kristallogr. Mineral.,* 1901, **34**, 449.

13 D. Turnbull and R.E. Cech, *J. Appl. Phys*. 1950, **21**, 1022-1028.

14 F. Meldrum and H. Colfen, *Chem. Rev*. 2008, **108**, 4332-4432.

15 Y. Yin, R.M. Rioux, C.K. Erdonmez, S. Hughes, G.A. Somorjai and A.P. Alivisatos, *Science,* 2004, **304** , 711-714.

16 (a) P. Tartaj, T. González-Carreño and C.J. Serna, *Langmuir,* 2002, **18** , 4556-4558; (b) X.Y. Tan, Y.T. Liu and K. Li, *AIChE Journal*, 2005, **51**, 1991-2000.

17 W. Zhao, J. Gu, L. Zhang, H. Chen and J. Shi, *J. Am. Chem. Soc.*, 2005, **127**, 8916-8917.

18 Y.G. Guo, J.S. Hu and L.J. Wan, *Adv. Mater.*, 2008, **20**, 2878-2887.

19 X.W. Lou, L.A. Archer and Z. Yang, *Adv. Mater.*, 2008, **20**, 3987-4019.

20 F. Caruso, R.A. Caruso and H. Mohwald, *Science*, 1998, **282**, 1111-1114.

21 F. Caruso, *Chem.-Eur. J.*, 2000, **6**, 413-419.

22 R.A. Caruso, A. Susha and F. Caruso, *Chem. Mater.*, 2001, **13**, 400-409.

23 K.H. Rhodes, S.A. Davis, F. Caruso, B. Zhang and S. Mann, *Chem. Mater.*, 2000, **12**, 2832-2834.

24 (a) G.C. Chen, C.Y. Kuo and S.Y. Lu, *J. Am. Ceram. Soc.*, 2005, **88**, 277-283; (b) F. Caruso, X. Shi, R.A. Caruso and A. Susha, *Adv. Mater.*, 2001, **13**, 740-744.

25 C.J. Martinez, B. Hockey, C.B. Montgomery and S. Semancik, *Langmuir*, 2005, **21**, 7937-7944.

26 Z. Liang, A. Susha and F. Caruso, *Chem Mater.*, 2003, **15**, 3176-3183.

27 M.A. Correa-Duarte, A. Kosiorek, W. Kandulski, M. Giersig and L.M. Liz-Marzán, *Chem. Mater.*, 2005, **17**, 3268-3272.

28 (a) I.D. Hosein and C.M. Liddell, *Langmuir*, 2007, **23**, 2892-2897; (b) K.P. Velikov and A. van Blaaderen, *Langmuir*, 2001, **17**, 4779-4786.

29 A. Wolosiuk, O. Armagan and P.V. Braun, *J. Am. Chem. Soc.*, 2005, **127**, 16356-16357.

30 L. Lu, G. Sun, S. Xi, H. Wang, H. Zhang, T. Wang and X. Zhou, *Langmuir*, 2003, **19**, 3074-3077.

31 (a) C. Zimmermann, C. Feldmann, M. Wanner and D. Gerthsen, *Small*, 2007, **3**, 1347-1349; (b) N. Yonghong, A. Tao, G. Hu, X. Cao, X. Wei and Z. Yang, *Nanotechnology*, 2006, **17**, 5013.

32 (a) J. Han, G. Song and R. Guo, *Adv. Mater*., 2006, **18**, 3140-3144; (b) A.M. Collins, C. Spickermann and S. Mann, *J. Mater. Chem*., 2003, **13**, 1112-1114.

33 D.H.M. Buchold and C. Feldmann, *Nano Letters*, 2007, **7**, 3489-3492.

34 C.I. Zoldesi and A. Imhof, *Adv. Mater*., 2005, **17**, 924-928; (b) C.L. Zoldesi, C.A. van Walree and A. Imhof, *Langmuir*, 2006, **22**, 4343-4352.

35 Z. Wang, M. Chen and L. Wu, *Chem. Mater*., 2008, **20**, 3251-3253.

36 J. Changlong, Z. Wangqun, G. Zou, W. Yu and Q. Yitai, *Nanotechnology*, 2005, **16**, 551.

37 Y.S. Han, G. Hadiko, M. Fuji and M. Takahashi, *Chem. Lett*., 2005, **34**, 152-153.

38 H. Hou, Q. Peng, S. Zhang, Q. Guo and Y. Xie, *Eur. J. Inorg. Chem*., 2005, **13**, 2625-2630.

39 C.Z. Wu, Y. Xie, L.Y. Lei, S.Q. Hu and C.Z. OuYang, *Adv. Mater*., 2006, **18**, 1727-1732.

40 C.P. Whitby, A.M. Djerdjev, J.K. Beattie and G.G. Warr, *Langmuir*, 2006, **23**, 1694-1700.

41 K.N. Tu and U. Gosele, *Appl. Phys. Lett*., 2005, **86**, 93111.

42 J. Gao, B. Zhang, X. Zhang and B. Xu, *Angew. Chem. Int. Edit.*, 2006, **45**, 1220-1223.

43 R.K. Chiang and R.T. Chiang, *Inorg. Chem*., 2006, **46**, 369-371.

44 H. Tan, S. Li and W.Y. Fan, *J. Phys. Chem. B*, 2006, **110**, 15812-15816.

45 (a) Y. Sun, B.T. Mayers and Y. Xia, *Nano Letters*, 2002, **2**, 481-485; (b) Y. Yin, C. Erdonmez, S. Aloni and A.P. Alivisatos, *J. Am. Chem. Soc*., 2006, **128**, 12671-12673.

46 S. Guo, Y. Fang, S. Dong and E. Wang, *J. Phys. Chem. C*, 2007, **111**, 17104-17109.

47 H.P. Liang, H.M. Zhang, J.S. Hu, Y.G. Guo, L.J. Wan and C.L. Bai, *Angew. Chem. Int. Edit*., 2004, **43**, 1540-1543.

48 H.P. Liang, L.J. Wan, C.L. Bai and L. Jiang, *J. Phys. Chem. B*, 2005, **109**, 7795-7800.

49 H.P. Liang, Y.G. Guo, H.M. Zhang, J.S. Hu, L.J. Wan and C.L. Bai, *Chem. Comm*., 2004, **13**, 1496-1497.

50 (a) Y. Chen, H. Chen, L. Guo, Q. He, F. Chen, J. Zhou, J. Feng and J. Shi, *ACS Nano*, 2009, **4**, 529-539; (b) S. Kobayashi, K. Hanabusa, N. Hamasaki, M. Kimura, H. Shirai and S. Shinkai, *Chem. Mater.*, 2000, **12**, 1523-1525; (c) L. Wang, T. Sasaki, Y. Ebina, K. Kurashima and M. Watanabe, *Chem. Mater.*, 2002, **14**, 4827-4832.

51 (a) N. Dhas and K. Suslick, *J. Am. Chem. Soc*., 2005, **127**, 2368-2369; (b) S.Y. Chang, L. Liu and S.A. Asher, *J. Am. Chem. Soc*., 1994, **116**, 6745-6747; (c) X. Lu, L. Au, J. McLellan, Z.Y. Li, M. Marquez and Y. Xia, *Nano Letters*, 2007, **7**, 1764-1769.

52 W. Wei, G.H. Ma, G. Hu, D. Yu, T. McLeish, Z.G. Su and Z.Y. Shen, *J. Am. Chem. Soc*., 2008, **130**, 15808-15810.

53 M. Burkatovskaya, G.P. Tegosa, E. Swietlika, T.N. Demidova, A.P. Castano and M.R. Hamblin, *Biomaterials*, 2006, **27**, 4157-4164.

54 M. Zhang, T. Tan, H. Yuan and C. Rui, *Compat. Pol*., 2003, **18**, 391-400.

55 (a) Y. He, Z. Li, P. Simone and T.P. Lodge, *J. Am. Chem. Soc.,* 2006, **128**, 2745-2750; (b) N. Kimizuka and T. Nakashima, *Langmuir*, 2001, **17**, 6759-6761.

56 R.P. Swatloski, S.K. Spear, J.D. Holbrey and R.D. Rogers, *J. Am. Chem. Soc*., 2002, **124**, 4974-4975.

57 H.B. Xie, S.B. Zhang and S.H. Li, *Green Chem.*, 2006, **8**, 630-633.

58 D.M. Phillips, L.F. Drummy, D.G. Conrady, D.M. Fox, R.R. Naik, M.O. Stone, P.C. Trulove, H.C. DeLong and R.A. Mantz, *J. Am. Chem. Soc.*, 2004, **126**, 14350-14351.

59 D. Zhao, L. Liao and Z. Zhang, *Clean-Soil,Air,Water*, 2007, **35**, 42-48.

60 Y.X. Gao, S.H. Yu, H. Cong, J. Jiang, A.W. Xu, W.F. Dong and H. Colfen, *J. Phys. Chem*., 2006, **110**, 6432-6436.

61 W. Dong, H. Cheng, Y. Yao, Y. Zhou, G. Tong, D. Yan, Y. Lai and W. Li, *Langmuir*, 2011, **17**, 366-370.

62 J. Bozzola and L. Russell, *Electron Microscopy: Principles and Techniques for Biologists*, Sudbury: Jones and Bartlett Publishers, 1999, 17-208.

63 M. Hoppert, *Microscopic Techniques in Biotechnology*, 1st ed., Weinheim: Wiley, 2003, 147-192.

64 F. Krumeich, *Bragg's Law of Diffraction*, 14 Jan. 2009, Web. 15 Feb. 2011.

65 V. Pecharsky and P. Zavalij, *Fundamentals of Powder Diffraction and Structural Characterization of Materials*, 2nd ed. New York: Springer, 2009, 142-144.

66 B.E. Warren, *X-Ray Diffraction*, New York: Dover Publications, 1990, 75-83.

67 J. Frank, *Electron Tomography,* 2nd ed. New York: Springer, 2006, 1-13.

68 R.A. Nyquist and C.L. Putzig., Infrared Spectroscopy, *Encyclopedia of Analytical Science*, Ed. A. Townshend, Vol. 4, San Diego: Academic Press, 1995, 2153-2170.

69 J.O. Hill, Thermogravimetry, *Encyclopedia of Analytical Science*, Ed. A. Townshend, Vol. 8, San Diego: Academic Press, 1995, 5141-5143.

70 B.D. Cullity and S.R. Stock, *Elements of X-ray diffraction*, 3rd ed. London: Prentice-Hall International, 2001, 1-664.

71 Z. Budrovic, H. Van Swygenhoven, P.M. Derlet, S. Van Petegem and B. Schmitt, *Science*, 2004, **304**, 273-276.

72 M.J. McAllister, J.L. Li, D.H. Adamson, H.C. Schniepp, A.A. Abdala, J. Liu, M. Herrera-Alonso, D.L. Milius, R. Car, R.K. Prud'homme and I.A. Aksay, *Chem. Mater.*, 2007, **19**, 4396-4404.

73 *1-Butyl-3-methylimidazolium chloride*, chemicalbook.com, Chembook, n.d. Web. 15 Feb. 2011.

74 S. Mann, B.R. Heywood, S. Rajam and J.B.A. Walker, 1991, *J. Phys. D: Appl. Phys.*, **24**, 154-164.

75 (a) H. Sugihara, K. Ono, K. Adachi, Y. Setoguchi, T. Ishihara and Y. Takita, *J. Ceram. Soc. Jpn.*, 1996, **104**, 832; (b) H. Sughiara, T. Ana, K. Adachi, A. Baba, N.

Egashira, H. Nishiguchi, T. Ishihara and Y. Takita, *J. Ceram. Soc. Jpn.*, 1997, **105**, 866.

76 T. Kato, A. Sugawara and N. Hosoda, *Adv. Mater.*, 2002, **14**, 869-877.

77 C.H. Lu, L.M. Qi, H.L. Cong, X.Y. Wang, J.H. Yang, L.L. Yang, D.Y. Zhang, J.M. Ma and W.X. Cao, *Chem. Mater.*, 2005, **17**, 5218–5224.

78 J. Aizenberg, S. Albeck, S. Weiner and L. Addadi, *J. Crystal Growth*, **142**, 1994, 156-164.

79 A. Berman, L. Addadi, A. Kvick, L. Leiserowitz, M. Nelson and S. Weiner, *Science*, 1990, **250**, 664-667.

80 J. Aizenberg, J. Hanson, M. Ilan, L. Leiserowitz, T.F. Koetzle, L. Addadi and S. Weiner, *FASEB J.*, 1995, **9**, 262-268.

81 M.F. Butler, N. Glaser, A.C. Weaver, M. Kirkland and M. Heppenstall-Butler, *Cryst. Growth Des.*, 2006, **6**, 781-794.

82 M. Kuman, *React. Funct. Polym.,* 2000, **46**, 1-27.

83 L. Qi, J. Li and J. Ma, *Adv. Mater*., 2002, **14**, 300-303.

84 J. Goldberger, R. He, Y. Zhang, S. Lee, H. Yan, H.J. Choi and P. Yang, *Nature*, 2003, **422**, 599-602.

85 J. Yu, H. Guo, S.A. Davis and S. Mann, *Adv. Funct. Mater*., 2006, **16**, 2035–2041.

86 (a) T.G. Baird, A.G. Cairns-Smith and D.S. Snell, *J. of Colloid and Interface Sci*., 1975, 50, 387-391; (b) D.J. Ahn, A. Berman and D. Charych, *J. Phys. Chem.,*1996, **100**, 12455-12461.

87 A. Pawlak and M. Mucha, *Thermochimica Acta*, 2003, **396**, 153-166.

88 (a) R. Bodmeier and O. Paeratakul, *J. Pharm. Sci.*, 1989, **11**, 964-967; (b) C. Qin, H. Li, Q. Xiao, Y. Liu, J. Zhu and Y. Du, *Carbohyd. Polym.*, 2006, **63**, 367-374.

89 L. Sun, L.J. Kepley and R.M. Crooks, *Langmuir*, 1992, **8**, 2101-2103.

90 (a) R.G. Nuzzo, L.H. Dubois and D.L. Allara, *J. Am. Chem. Soc.,* 1990, **112**, 558-569; (b) L.J. Bellamy, *The Infrared Spectra of Complex Molecules*, 3rd ed., London: Chapman & Hall, 1975.

91 L. Treccani, K. Mann, F. Heinemann and M. Fritz, *Biophys. J*., 2006, **91**, 2601-2608.

92 A.P. Wheeler, J.W. George and C.A. Evans, *Science*, 1982, **212**, 1397-1398.

93 (a) V.N. Kalashnikov, *J. Rheol*., 1994, **38**, 1385-1403; (b) E.R. Morris, A.N. Cutler, S.B. Ross-Murphy and D.A. Rees, *Carbohydrate Polymers*, 1981, **1**, 5-21.

94 E.J. Zeller and J.L. Wray, *Am. Assoc. of Petr. Geol.,* 1956, **40**, 140-152.

95 E.A. Burton and L.M. Walter, *Geology*, 1987, **15**, 111-114.

96 J.F. Chen, J.X. Wang, R.J. Liu, L. Shao and L.X. Wen, *Inorg. Chem. Comm.*, 2004, **7**, 447-449.

97 J.X. Wang, L.X. Wen, R.J. Liu and J.F. Chen, *J. Solid State Chem*., 2005, **178**, 2383-2389.

98 M. Li and S. Mann, *Adv. Funct. Mater*. 2002, **12**, 773-779.

99 J. Rieger, J. Thieme and C. Schmidt, *Langmuir*, 2000, **16**, 8300-8305.

100 S. Albeck, S. Weiner and L. Addadi, *Chem. Eur.*, 1996, **2**, 278-284.

101 A.W. Xu M. Antonietti, H. Colfen and Y.P. Fang, *Adv. Funct. Mater*., 2006, **16**, 903-908.

VITA

Name:	Hsingming Anna Chen
Address:	Texas A&M University Department of Chemical Engineering Jack E. Brown Engineering Bldg. 3122 TAMU, Room 411 College Station, TX 77843
Email Address:	hachen1@neo.tamu.edu
Education:	B.S., Chemical Engineering, The University of Texas, 2005 M.S., Chemical Engineering, Texas A&M University, 2011